



Assessment of lidar depolarization uncertainty by means of a polarimetric lidar simulator

Juan Antonio Bravo-Aranda^{1,2,3}, Livio Belegante⁴, Volker Freudenthaler⁵, Lucas Alados-Arboledas^{1,2}, Doina Nicolae⁴, María José Granados-Muñoz^{1,2}, Juan Luis Guerrero-Rascado^{1,2}, Aldo Amodeo⁶, Giusseppe D'Amico⁶, Ronny Engelmann⁷, Gelsomina Pappalardo⁶, Panos Kokkalis⁸, Rodanthy Mamouri⁹, Alex Papayannis⁸, Francisco Navas-Guzmán^{1,2,a}, Francisco José Olmo^{1,2}, Ulla Wandinger⁷, Francesco Amato⁶, and Martial Haeffelin³

¹ Andalusian Institute for Earth System Research (IISTA-CEAMA), Granada, Spain

² Dpt. Applied Physics, University of Granada, Granada, Spain

³ Institute Pierre-Simon Laplace, CNRS-Ecole Polytechnique, Paris, France

⁴ National Institute of Research & Development for Optoelectronics – INOE 2000,

Magurele, Ilfov, Romania

⁵ Ludwig-Maximilians-Universität Meteorologisches Institut, München, Germany

⁶ Consiglio Nazionale delle Ricerche Istituto di Metodologie per l'Analisi Ambientale

I.M.A.A. – C.N.R., Potenza, Italy

⁷ Leibniz Institute for Tropospheric Research (TROPOS), Permoserstr. 15,

04318 Leipzig, Germany

⁸ Laser Remote Sensing Unit, National Technical University of Athens, Physics Dept.,

15780 Zografou, Greece

⁹ Department of Civil Engineering and Geomatics, Cyprus University Of Technology,
Lemesos, Cyprus

^anow at: Institute of Applied Physics (IAP), University of Bern, Bern, Switzerland

Correspondence to: Juan Antonio Bravo-Aranda (jabravo@ugr.es)

Received: 4 November 2015 – Published in Atmos. Meas. Tech. Discuss.: 8 February 2016

Revised: 7 July 2016 – Accepted: 14 July 2016 – Published: 7 October 2016

Abstract. Lidar depolarization measurements distinguish between spherical and non-spherical aerosol particles based on the change of the polarization state between the emitted and received signal. The particle shape information in combination with other aerosol optical properties allows the characterization of different aerosol types and the retrieval of aerosol particle microphysical properties. Regarding the microphysical inversions, the lidar depolarization technique is becoming a key method since particle shape information can be used by algorithms based on spheres and spheroids, optimizing the retrieval procedure. Thus, the identification of the depolarization error sources and the quantification of their effects are crucial. This work presents a new tool to assess the systematic error of the volume linear depolarization ratio (δ), combining the Stokes–Müller formalism and the

complete sampling of the error space using the lidar model presented in Freudenthaler (2016a). This tool is applied to a synthetic lidar system and to several EARLINET lidars with depolarization capabilities at 355 or 532 nm. The lidar systems show relative errors of δ larger than 100 % for δ values around molecular linear depolarization ratios (~ 0.004 and up to ~ 10 % for $\delta = 0.45$). However, one system shows only relative errors of 25 and 0.22 % for $\delta = 0.004$ and $\delta = 0.45$, respectively, and gives an example of how a proper identification and reduction of the main error sources can drastically reduce the systematic errors of δ . In this regard, we provide some indications of how to reduce the systematic errors.

1 Introduction

The lidar depolarization technique is a useful tool for different applications in atmospheric science, such as the identification of the thermodynamic phase of clouds (e.g. Ansmann et al., 2005; Reichardt et al., 2003; Schotland et al., 1971) and the aerosol typing (e.g. Bravo-Aranda et al., 2013; Groß et al., 2011, 2012, 2013, 2015; Navas-Guzmána, b et al., 2013). Additionally, the lidar depolarization technique is very important for improving the retrieval of microphysical aerosol properties (e.g. Ansmann et al., 2011; Chaikovsky et al., 2002; Granados-Muñoz et al., 2014; Wagner et al., 2013; Samaras et al., 2015), becoming crucial for inversion algorithms based on modelling aerosol particles as spheres and spheroids. Unfortunately, the reliability of the lidar depolarization technique is limited due to the complexity of the depolarization calibration.

A relative polarization calibration using molecular depolarization as a reference introduces a high uncertainty due to possibly residual depolarizing aerosol in the assumed clean air range and due to the low signal-to-noise ratio. Absolute calibration methods are more robust, but often do not take into account all polarization effects of the lidar optics, as e.g. the polarization-dependent receiver transmission (Matis et al., 2009). Many authors have focussed their effort on the improvement of the lidar polarization calibration and on the determination of the depolarization uncertainties (e.g. Álvarez et al., 2006; David et al., 2012; Bravo-Aranda et al., 2013; Hayman and Thayer, 2012; Freudenthaler et al., 2009; Freudenthaler, 2016a). The identification of the lidar optics' influence on the depolarization measurements is relevant (i) for an appropriate assessment of depolarization ratio errors, (ii) for the prioritization of the technical improvements of the lidars according to the optical parameters with the larger impact on depolarization ratio errors, and (iii) for the development of future lidar generations. To this end, the Stokes–Müller formalism is used to provide the theoretical framework and the formulae for the polarization calibration factor covering the different calibration techniques and lidar set-ups used in this work (Freudenthaler, 2016a).

This work quantifies the volume linear depolarization ratio uncertainty ($\Delta\delta$) due to the unknown systematic errors caused by the uncertainties of the polarization-relevant parameters of the lidar optics and assesses the contribution of each lidar functional block to the total uncertainty. A software tool called Polarimetric Lidar Simulator (PLS) has been developed, based on the theoretical framework presented by Freudenthaler (2016a), which performs a complete search of the error space. The PLS is applied to several lidar systems in order to show the dependence of the systematic error on their design features. Random errors due to signal noise are neglected in this work. Their contribution to the uncertainty can be derived, in a similar way to Pappalardo et al. (2004) and Guerrero-Rascado et al. (2008), by simulating the com-

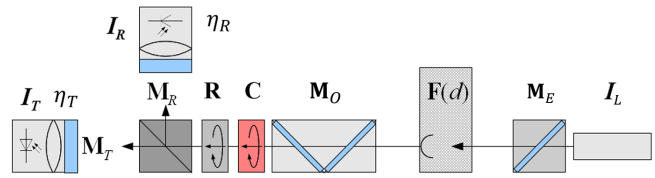


Figure 1. Lidar scheme based on functional blocks (adapted from Freudenthaler, 2016a). From right to left: laser (I_L), steering optics (M_E), atmosphere (F), receiving optics (M_O), calibrator (C), additional rotation of the PBS by 90° (R), polarizing beam-splitter cube (transmitted (T) and reflected (R) matrices, M_T and M_R), and the transmitted (T) and reflected (R) signals (I_T and I_R).

plete error space of δ due to the uncertainties of the lidar parameters.

In Sect. 2 we describe the functional blocks. In Sect. 3, the PLS performance is explained in detail. In Sect. 4 a synthetic lidar set-up is used to identify the most important error sources. In Sect. 5, the total systematic error of $\Delta\delta$ is determined for several EARLINET lidar systems, the error sources are analysed, and possible ways to reduce the uncertainties are pointed out. Finally, conclusions are reported in Sect. 6.

2 Basis of the Polarimetric Lidar Simulator (PLS): Stokes–Müller formalism applied to lidar functional blocks

As described by Freudenthaler (2016a), we subdivide our lidar system model into functional blocks with the corresponding Stokes vector and Müller matrices: the laser I_L , the emitting optics M_E (beam expander, steering mirrors), the receiving optics M_O (telescope, collimator, dichroic mirrors ...), and the polarizing beam splitter M_S including the detectors. M_S is further split into the transmitted path M_T and the reflected path M_R with the corresponding Stokes vectors I_T and I_R . Furthermore, the polarization calibrator C can be considered as an additional functional block. Figure 1 shows a scheme of the lidar based on the functional blocks. We also include a rotator R to enable different lidar set-ups as described below. The next sections explain each functional block, describe the assumptions, and show their Stokes vectors or Müller matrices.

2.1 Laser, I_L

The specified “polarization purity” of lasers commonly used in lidars is of the order of 100 : 1, if it is specified at all. Already the terminology indicates that such specifications are rather vague. Actually, laser manufacturers do not measure the state of polarization of the laser beams, and seem to give values which are on the safe side under all circumstances. Theoretically, non-linear crystals as second and third harmonic generators should provide very clean linear polariza-

tion, just depending on the quality and accuracy of alignment of the crystals. Due to a lack of detailed information we neglect this source of errors in this work. However, in order to remove this uncertainty, in some lidar systems high-quality polarizing beam splitters are used to improve the degree of linear polarization of the emitted laser beams. In both cases, the plane of polarization of the laser beam can be rotated by angle α with respect to the incident plane of the polarizing beam splitter in the receiver optics, which results in the Stokes vector \mathbf{I}_L of the emitted laser beam:

$$\mathbf{I}_L = I_L \begin{pmatrix} 1 \\ \cos(2\alpha) \\ \sin(2\alpha) \\ 0 \end{pmatrix}, \quad (1)$$

where I_L is the laser energy.

2.2 Laser emitting optics, \mathbf{M}_E

The emitting functional block can consist of a set of dichroic beam splitters and steering mirrors, which align the laser beam with the telescope axis, and optionally includes beam expanders to decrease the emitted beam divergence and for eye safety reasons. The depolarizing effect of beam expanders is neglected, since we cannot estimate the uncertainties introduced by possible birefringence as in the case of CaF₂ lenses of apochromatic beam expanders. In addition, stress birefringence in windows in the transmitting part (e.g. roof window) is neglected due to its complex analysis and lack of information. The effect of these optical devices has to be investigated in the future.

The general Müller matrix of dichroic beam splitters and steering mirrors is (Lu and Chipman, 1996; Freudenthaler, 2016a)

$$\mathbf{M} = T \begin{pmatrix} 1 & D & 0 & 0 \\ D & 1 & 0 & 0 \\ 0 & 0 & Z\cos(\Delta) & Z\sin(\Delta) \\ 0 & 0 & -Z\sin(\Delta) & Z\cos(\Delta) \end{pmatrix}, \quad (2)$$

where T and D are the non-polarized transmittance and the diattenuation parameter (Chipman, 2009), respectively, defined by

$$T = \frac{T^p + T^s}{2} \quad (3)$$

$$D = \frac{T^p - T^s}{T^p + T^s}, \quad (4)$$

with T^p and T^s as the parallel and perpendicular intensity transmission coefficients (transmittances) with respect to the incident plane. The phase shift between the parallel (φ^p) and the perpendicular (φ^s) components, hereafter called retardance, is noted by

$$\Delta = \varphi^p - \varphi^s, \quad (5)$$

and Z is given by

$$Z = \sqrt{1 - D^2}. \quad (6)$$

Mirrors include an additional 180° retardance.

If the emitting optics is formed by different steering/dichroic mirrors, the Müller matrix of the emitting optics block \mathbf{M}_E is the matrix product of the individual matrices as

$$\mathbf{M}_E = \mathbf{M}_1 \mathbf{M}_2 \dots \mathbf{M}_n = \prod_i \mathbf{M}_i, \quad (7)$$

where the subscript $i = \{1, 2, \dots, n\}$ indicates number of steering/dichroic mirrors. We assume that all the elements in a functional block are aligned perfectly with respect to each other, and with that an effective Müller matrix of the emitter optics \mathbf{M}_E can be obtained from Eq. (2) as follows:

$$\mathbf{M}_E = T_E \begin{pmatrix} 1 & D_E & 0 & 0 \\ D_E & 1 & 0 & 0 \\ 0 & 0 & Z_E\cos(\Delta_E) & Z_E\sin(\Delta_E) \\ 0 & 0 & -Z_E\sin(\Delta_E) & Z_E\cos(\Delta_E) \end{pmatrix}, \quad (8)$$

where T_E , D_E , and Δ_E are the effective transmittance, diattenuation parameter, and retardance of \mathbf{M}_E . For example, considering an emitting functional block made of two dichroic mirrors (\mathbf{M}_1 and \mathbf{M}_2), \mathbf{M}_E is given by

$$\mathbf{M}_E = T_{12} \begin{pmatrix} 1 & D_{12} & 0 & 0 \\ D_{12} & 1 & 0 & 0 \\ 0 & 0 & Z_{12}\cos(\Delta_{12}) & Z_{12}\sin(\Delta_{12}) \\ 0 & 0 & -Z_{12}\sin(\Delta_{12}) & Z_{12}\cos(\Delta_{12}) \end{pmatrix}, \quad (9)$$

where T_{12} , D_{12} , Z_{12} , and Δ_{12} are

$$T_{12} = T_1 T_2 (1 + D_1 D_2) \quad (10)$$

$$D_{12} = \frac{D_1 + D_2}{1 + D_1 D_2} \quad (11)$$

$$Z_{12} = \frac{Z_1 Z_2}{1 + D_1 D_2} \quad (12)$$

$$\Delta_{12} = \Delta_1 + \Delta_2, \quad (13)$$

where T , D , Z , and Δ subscripted by 1 and 2 are the parameters of \mathbf{M}_1 and \mathbf{M}_2 according to Eq. (8).

This process can be applied iteratively to obtain the effective Müller matrix, \mathbf{M}_E composed of more than two elements.

While we assume the absence of rotational misalignments between the elements inside a block, we consider a rotational misalignment of the whole functional block with respect to the incident plane of the polarizing beam splitter (PBS). To this end, the rotation Müller matrix \mathbf{R} is defined by

$$\mathbf{R}(\beta) = \begin{pmatrix} 1 & 0 & 0 & 0 \\ 0 & \cos(2\beta) & -\sin(2\beta) & 0 \\ 0 & \sin(2\beta) & \cos(2\beta) & 0 \\ 0 & 0 & 0 & 1 \end{pmatrix}, \quad (14)$$

where the angle β describes the rotational misalignment of \mathbf{M}_E with respect to the PBS incident plane. Thus,

$$\mathbf{M}_E(\beta) = \mathbf{R}(\beta) \mathbf{M}_E \mathbf{R}(-\beta), \quad (15)$$

resulting in

$$\mathbf{M}_E(\beta) = T_E \quad (16)$$

$$\begin{pmatrix} 1 & D_E \cos(2\beta) & D_E \sin(2\beta) & 0 \\ D_E \cos(2\beta) & (1 - W_E \sin^2(2\beta)) & W_E \sin(2\beta) \cos(2\beta) & -Z_E \sin(\Delta_E) \sin(2\beta) \\ D_E \sin(2\beta) & W_E \sin(2\beta) \cos(2\beta) & (1 - W_E \cos^2(2\beta)) & Z_E \sin(\Delta_E) \cos(2\beta) \\ 0 & Z_E \sin(\Delta_E) \sin(2\beta) & -Z_E \sin(\Delta_E) \cos(2\beta) & Z_E \cos(\Delta_E) \end{pmatrix},$$

with $W_E = 1 - Z_E \cos(\Delta_E)$.

The polarization effect of \mathbf{M}_E is described by the effective diattenuation parameter (D_E), the effective retardance (Δ_E), and the rotational misalignment angle β of the whole functional block with respect to the PBS polarizing plane. The possible effect of tilted scanning mirrors on depolarization measurements was highlighted by Bissonnette et al. (2001).

2.3 Receiving optics, \mathbf{M}_O

This functional block, formed by the telescope and dichroic beam splitters, leads the received signal to the photomultipliers and, in case of multiwavelength lidar, separates the received signal by wavelength. In the same way as the emitting optics, \mathbf{M}_O can be described by a unique effective Müller matrix as follows:

$$\mathbf{M}_O(\gamma) = T_O \quad (17)$$

$$\begin{pmatrix} 1 & D_O \cos(2\gamma) & D_O \sin(2\gamma) & 0 \\ D_O \cos(2\gamma) & (1 - W_O \sin^2(2\gamma)) & W_O \sin(2\gamma) \cos(2\gamma) & -Z_O \sin(\Delta_O) \sin(2\gamma) \\ D_O \sin(2\gamma) & W_O \sin(2\gamma) \cos(2\gamma) & (1 - W_O \cos^2(2\gamma)) & Z_O \sin(\Delta_O) \cos(2\gamma) \\ 0 & Z_O \sin(\Delta_O) \sin(2\gamma) & -Z_O \sin(\Delta_O) \cos(2\gamma) & Z_O \cos(\Delta_O) \end{pmatrix},$$

where T_O , D_O , and Δ_O are the effective transmittance, diattenuation, and retardance of \mathbf{M}_O , respectively, and γ describes the rotational misalignment angle of \mathbf{M}_O with respect to the incident plane of the PBS. The polarization effects of telescopes with small incidence angles of the light beam are neglected in this work. This approximation is valid for Cassegrain telescopes, but possibly not for Newtonian telescopes with 90° fold mirrors (Clark and Breckinridge, 2011; Di et al., 2015; Lam and Chipman, 2015) as in the case of the PollyXT lidars (Engelmann et al., 2016). This source of error has to be investigated further. Furthermore, windows commonly used to protect the telescope can also affect the polarization due to intrinsic and stress birefringence, but this is also not considered in the simulator since the effect is very difficult to evaluate due to the lack of information about the properties and the time-dependent behaviour.

2.4 Polarizing beam splitters (\mathbf{M}_R and \mathbf{M}_T)

A polarizing splitter separates the received signal into reflected and transmitted signals. Consequently, two Müller matrices are required to describe the reflection (\mathbf{M}_R) and transmission (\mathbf{M}_T) processes. Due to the similarity in the shape of the matrices, both matrices can be described by one matrix with the subscript $S = \{R, T\}$ with \mathbf{M}_S as follows:

$$\mathbf{M}_S = T_S \begin{pmatrix} 1 & D_S & 0 & 0 \\ D_S & 1 & 0 & 0 \\ 0 & 0 & Z_S \cos(\Delta_S) & Z_S \sin(\Delta_S) \\ 0 & 0 & -Z_S \sin(\Delta_S) & Z_S \cos(\Delta_S) \end{pmatrix}, \quad (18)$$

where Δ_S is the phase shift of \mathbf{M}_S , T_S , D_S are defined by

$$T_S = \frac{T_S^P + T_S^S}{2} \quad (19)$$

$$D_S = \frac{T_S^P - T_S^S}{T_S^P + T_S^S}, \quad (20)$$

with T_S^P and T_S^S as the parallel p and perpendicular s transmittance/reflectance, respectively, and $Z_S = \sqrt{1 - D_S}$. Parallel and perpendicular polarization is defined with respect to the incidence plane of the polarizing beam splitter. We attribute any polarization-independent absorption to the channel gain (see Sect. 2.6) and get therewith

$$T_S^P + T_S^S = 1. \quad (21)$$

Ideal PBS split light in the two orthogonally polarized components without crosstalk, which means $R_p = T_s = 0$. But real PBS always transmit a fraction of the perpendicular polarization and reflect part of parallel polarization. This effect of the crosstalk on the linear depolarization ratio has been studied for example by Álvarez et al. (2006), Freudenthaler et al. (2009), and Snels et al. (2009). As shown in Freudenthaler (2016a), it is relatively easy to reduce the crosstalk by adding polarizer sheet filters after the PBS. The Müller matrix of the cleaned PBS, $\mathbf{M}_S^\#$, is

$$\mathbf{M}_S^\# = T_S^\# \begin{pmatrix} 1 & D_S^\# & 0 & 0 \\ D_S^\# & 1 & 0 & 0 \\ 0 & 0 & 0 & 0 \\ 0 & 0 & 0 & 0 \end{pmatrix}, \quad (22)$$

where $D_S^\# = \{D_T^\# = 1, D_R^\# = -1\}$ and the superscript “ $\#$ ” indicates that the PBS is “cleaned”.

We assume that the extinction ratio of the cleaning polarizing sheet filters is sufficiently small and that they can be oriented with an accuracy much better than $\pm 5^\circ$ with respect to the PBS, and that therefore the resulting error of the $D_S^\#$ can be neglected (See Appendix A).

2.5 Rotator, \mathbf{R}

The parallel polarized component of the emitted laser beam can be detected either in the transmitted or in the reflected path behind the PBS. This depends on the orientation Ψ of the PBS with respect to the laser polarization. We consider this by means of a rotator $\mathbf{R}(\psi)$ (Eq. 14) before the PBS (see Fig. 1). For $\Psi = 90^\circ$, the reflected and transmitted signals correspond to the parallel and perpendicular polarized components, respectively, and vice versa for $\Psi = 0^\circ$.

2.6 Photomultipliers, η_R , η_T

The reflected and transmitted signals are detected by the photomultipliers which perform the light-to-electrical signal conversion. They affect the depolarization measurements as,

in general, different photomultipliers have different gains. Regarding the Stokes–Müller formalism, we define the opto-electronic gains η_R and η_T for the photomultiplier gains of the transmitted and reflected signals including all optical attenuation of the lidar system in the transmitted and reflected path that is independent of polarization. We set them equal to 1 since we only investigate the polarization-dependent errors of the lidar optics.

2.7 Calibrator, C

The calibrator allows the determination of the polarization effect of the optical devices located behind the calibrator and of the gain ratio of the photomultipliers (PMTs). For the lidar set-up in Fig. 1, the calibration factor η includes the effects of the polarizing splitter (\mathbf{M}_R and \mathbf{M}_T) and photomultiplier gains, η_R and η_T :

$$\eta = \frac{\eta_R}{\eta_T} \frac{T_R}{T_T}. \quad (23)$$

Different calibration methods have been proposed either using the theoretical value of molecular depolarization (e.g. Cairo et al., 1999) or using additional optical devices as half-wave plates or polarization filters (e.g. Álvarez et al., 2006; Snels et al., 2009; Freudenthaler et al., 2009). Particularly, the $\Delta 90^\circ$ calibration method has been implemented within EARLINET lidar systems (e.g. Freudenthaler et al. 2009; Nemuc et al., 2013; Mamouri and Ansmann, 2014; Bravo-Aranda et al., 2015). This method uses two measurements, rotating the polarizing plane of the received signal at angles ϕ_1 and ϕ_2 around the nominal axial rotation (Ψ) with the constraint $|\phi_2 - \phi_1| = 90^\circ$ (e.g. $\phi_1 = 45^\circ, \phi_2 = -45^\circ$ around the measurement position $\Psi = 0^\circ$). These rotations allow the equalization of the reflected and transmitted signals and thus, any difference between the reflected and transmitted signals is only due to the polarizing effects of the optical devices between the calibrator and the photomultipliers. The equalization of the reflected and transmitted signals can be made by a physical rotation of the receiving optics including the photomultipliers, by rotating a half-wave plate placed before the PBS, or by using a linear polarizing filter rotated accordingly (see Freudenthaler, 2016a, for more details).

The measured calibration factor, η^* , is

$$\eta^*(\Psi, x45^\circ + \varepsilon) = \frac{\mathbf{I}_R(\Psi, x45^\circ + \varepsilon)}{\mathbf{I}_T(\Psi, x45^\circ + \varepsilon)}, \quad (24)$$

where the two rotation angles, ϕ_1 and ϕ_2 , are written as $x45^\circ + \varepsilon$, with $x = \pm 1$ indicating the rotational direction and ε taking the deviation from the nominal rotation into account. Then, their geometric mean,

$$\eta_{\sqrt{\pm}}^*(\Psi, \varepsilon) = \sqrt{\eta^*(\Psi, +45^\circ + \varepsilon) \eta^*(\Psi, -45^\circ + \varepsilon)}, \quad (25)$$

is calculated since it is less influenced by ε than $\eta^*(\Psi, x45^\circ + \varepsilon)$, as indicated by Freudenthaler et al. (2009).

It is possible to show (Freudenthaler, 2016a) that the analytical expressions of $\eta_{\sqrt{\pm}}^*(\Psi, \varepsilon)$, corresponding to a different experimental set-up, are always in the form

$$\begin{aligned} \eta_{\sqrt{\pm}}^*(\alpha, D_E, \Delta_E, \beta, D_O, \Delta_O, \gamma, \varepsilon, D_T, D_R) \\ = \eta f(\alpha, D_E, \Delta_E, \beta, D_O, \Delta_O, \gamma, \varepsilon, D_T, D_R), \end{aligned} \quad (26)$$

where $f(\alpha, D_E, \Delta_E, \beta, D_O, \Delta_O, \gamma, \varepsilon, D_T, D_R)$ is the combined influence of all the parameters which are not corrected by η . Hereafter, the correction factor, $f(\alpha, D_E, \Delta_E, \beta, D_O, \Delta_O, \gamma, \varepsilon, D_T, D_R)$, will be noted by $f(\alpha, \dots)$.

2.8 Reflected and transmitted signals, \mathbf{I}_R and \mathbf{I}_T

According to the Stokes–Müller formalism, the reflected (\mathbf{I}_R) and transmitted (\mathbf{I}_T) signals can be obtained by multiplying the laser beam Stokes vector (\mathbf{I}_L) by the subsequent Müller matrices, which represent the different functional blocks, and the atmosphere \mathbf{F} , which describes the scattering matrix for randomly oriented particles (van de Hulst, 1957; Mishchenko and Hovenier, 1995), by

$$\mathbf{F} = F_{11} \begin{pmatrix} 1 & 0 & 0 & 0 \\ 0 & a & 0 & 0 \\ 0 & 0 & -a & 0 \\ 0 & 0 & 0 & (1-2a) \end{pmatrix}, \quad (27)$$

where F_{11} is the backscatter coefficient and a is the polarization parameter. Both parameters are range-dependent, but since this dependency has no influence on our error calculation, we omitted it in the following. Please note that, instead of the polarization parameter a , different but equivalent expressions are used in other publications as described in more detail in Freudenthaler (2016a). Probably most known is the depolarization parameter $d = 1 - a$ used in Gimmesadt (2008).

With that, the Stokes vector of the lidar and calibration measurements is described by

$$\mathbf{I}_S(\Psi) = \eta_S \mathbf{M}_S \mathbf{R}(\Psi) \mathbf{M}_O \mathbf{F} \mathbf{M}_E \mathbf{I}_L \quad (28)$$

$$\mathbf{I}_S(\Psi, x45^\circ + \varepsilon) = \eta_S \mathbf{M}_S \mathbf{R}(\Psi) \mathbf{C}(x45^\circ + \varepsilon) \mathbf{M}_O \mathbf{F} \mathbf{M}_E \mathbf{I}_L, \quad (29)$$

where the first element of the Stokes vectors is the energy detected by the photomultipliers. Based on the Stokes–Müller formalism presented, the detected energy value depends on the 18 lidar parameters summarized in Table 1. However, only some of them are considered by PLS for the assessment of the error sources (see “error source” column in Table 1).

2.9 Volume linear depolarization ratio, δ

The volume linear depolarization ratio δ which contains the contributions of particles and air molecules, is directly related to the polarization parameter a by (Mishchenko and

Table 1. List of the functional blocks and lidar parameters used for describing the lidars. The error source column checks the parameters used for the assessment of the depolarization error.

Functional block			Parameters		Error source
Name	Symbol	Name		Symbol	
Laser	I_L	Laser intensity	I_L	α	No
		Misalignment angle of the plane of polarization of the laser*			Yes
Emitting optics	M_E	Effective diattenuation	D_E	Δ_E	Yes
		Effective retardance			Yes
		Effective misalignment angle*			Yes
Receiving optics	M_O	Effective diattenuation	D_O	Δ_O	Yes
		Effective retardance			Yes
		Effective misalignment angle*			Yes
Calibrator	C	Calibration angle	ϕ	ε	No
		Misalignment angle*			Yes
Polarizing splitter	M_S	Measurement angle	Ψ	D_T	No
		Parallel-polarized* light transmittance			Yes
		Perpendicular-polarized* light transmittance			
		Parallel-polarized* light reflectance		D_R	Yes
		Perpendicular-polarized* light reflectance			
		Photomultiplier gain factor for transmitted signal		T_T^P	No
		Photomultiplier gain factor for reflected signal		T_R^P	No

* with respect to the incident plane of the PBS.

Hovenier, 1995)

$$\delta = \frac{1-a}{1+a}. \quad (30)$$

For further details regarding mathematical expressions of depolarization parameters, see Cairo et al. (1999). δ can be retrieved from lidar measurements by the following general equation given by Freudenthaler (2016a):

$$\delta = \frac{\delta^*(G_T + H_T) - (G_R + H_R)}{(G_R - H_R) - \delta^*(G_T - H_T)}, \quad (31)$$

where the parameters G_T , G_R , H_T , and H_R are determined by solving the matrix multiplication of Eq. (24) and separating the measured energy I_S into terms with and without the polarization parameter, a , as follows:

$$I_S = G_S + aH_S, \quad (32)$$

(Further details are given by Freudenthaler, 2016.) and $\delta^*(\Psi)$ is the reflected-to-transmitted signal ratio divided by the calibration factor, η (Eq. 23):

$$\delta^*(\Psi) = \frac{1}{\eta} \frac{I_R(\Psi)}{I_T(\Psi)}, \quad (33)$$

, where η has to be derived from the measured gain ratio, $\eta_{\sqrt{\pm}}$ (Eq. 26), estimating $f(\alpha, \dots)$ either from information already available (e.g. from technical specifications) or from

additional measurements performed for this purpose (see Freudenthaler, 2016a). Without any information, we have to assume $f(\alpha, \dots) \cong 1$. Therefore, a better characterization of the lidar system through G_S , H_S , and $f(\alpha, \dots)$ decreases the systematic errors of the depolarization measurements.

3 Polarimetric Lidar Simulator (PLS) performance

To quantify the systematic error of the linear depolarization ratio, the Polarimetric Lidar Simulator (PLS) is developed based on the matrix equations resulting from the theoretical framework given by Freudenthaler (2016a) (see Sect. 2). Because the parameters involved in the simulation are not always independent, we use a complete grid sampling of the parameter error space to calculate all possibly measured signals by means of numerical matrix calculation (Eqs. 28 and 29) and correct each measurement for the polarization effects using the assumed real parameter values and the correction Eqs. (26) and (31). The steps of the PLS workflow are shown in Fig. 2 and explained in detail below.

1. Creation of a parametric model: the parameters are noted by x_1, \dots, x_n in Fig. 2 and listed in Table 1, and their uncertainties are either taken from the technical specifications of the optical devices, or assumed with reasonable values. Particularly, for the beam-splitter properties, the reflectance and transmittance coefficients require additional calculations according to the splitter

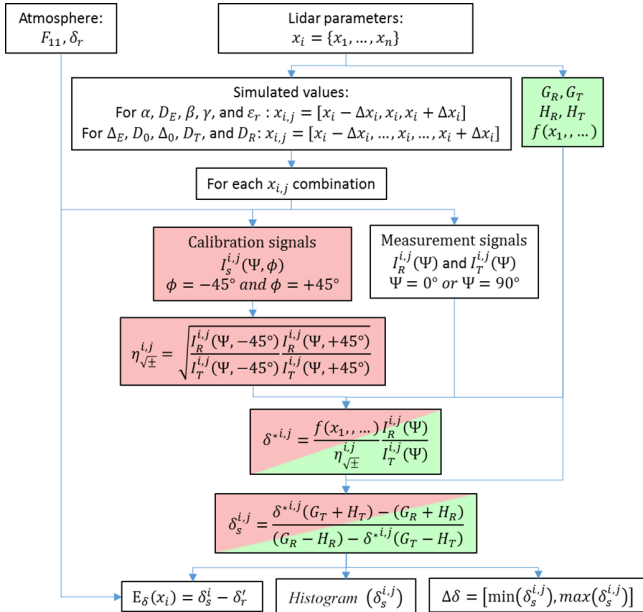


Figure 2. PLS flow chart. The steps of the polarization calibration are marked in red, whereas the correction steps applied with the assumed true parameters are marked in green. $x_1 \dots x_n$ are the lidar parameters from Table 1.

type. MULHACEN, RALI, and LB21 use commercial PBS, and thus the T_T^p and T_T^s values and the uncertainties from the technical specifications are used, whereas the values and uncertainties of T_R^p and T_R^s are calculated using equation Eqs. (20) and (21). MUSA, IPRAL, and POLIS (355 and 532 nm) use a cleaned PBS with $T_R^p = T_R^s = 1$ and $T_T^s = T_R^p = 0$. For POLLY-XT SEA, T_T^p and T_T^s values and uncertainties are obtained from the technical specifications. T_R^p is calculated by the means of the extinction ratio (ER) as $T_R^p = \text{ER} (1 - T_T^p)$, with the ER of the linear polarizer used to measure the perpendicular signal, and $T_R^s = 0$ assumed due to the high quality of the linear polarizer. Finally, the radiation-atmosphere interaction is simulated by the atmospheric parameters F_{11} (backscattering coefficient) and δ_r (real atmospheric δ) (see Sect. 2.8). Calculation of the correction factors, G_R, G_T, H_R, H_T , and $f(x_1, \dots)$ is based on the parameters values x_1, \dots, x_n .

2. Calculation of the correction factors, G_R, G_T, H_R, H_T , and $f(x_1, \dots)$, is based on the assumed real parameter values x_1, \dots, x_n .
3. Generation of simulated values: Gaussian or uniform distributions with a large number of random values (~ 100 or larger) are commonly used in order to obtain a reliable $\Delta\delta$. In our case, the parameter uncertainties are not related to random variations but to a lack of knowledge of the real value, and therefore a uniform distribution with a complete grid sampling is used

since all the combinations are equally probable. However, a large number of simulations for each parameter would lead to an unmanageable quantity of combinations, wherefore we adjust the number of iteration as follows.

- a. For the parameters $\alpha, D_E, \beta, \gamma$, and ε_r , we use only three values: $x_{i,j} = [x_i - \Delta x_i, x_i, x_i + \Delta x_i]$.
- b. For the parameters $\Delta_E, D_0, \Delta_0, D_T$, and D_R we use values between $x_i - \Delta x_i$ and $x_i + \Delta x_i$ which a fixed step calculated to provide around 10^6 combinations: $x_{i,j} = [x_i - \Delta x_i, \dots, x_i, \dots, x_i + \Delta x_i]$. Especially for Δ_E and Δ_0 , the steps are chosen dense enough to avoid aliasing effects.
4. Evaluation of the model for each $x_{i,j}$ combination and the atmospheric parameters, F_{11} and δ_r : to determine the influence of the atmospheric δ on the systematic error, this procedure is performed at δ_r values of 0.004 and 0.45 as representative values of the minimum and maximum atmospheric δ :
 - a. calibration and measurement signals $I_s^{i,j}(\Psi)$ and $I_s^{i,j}(\Psi, \phi)$;
 - b. calibration signals used to retrieve the calibration factor, $\eta_{\sqrt{\Xi}}^{i,j}$;
 - c. $\delta_s^{i,j}$ retrieved using $\eta_{\sqrt{\Xi}}^{i,j}$ and $f(\alpha, \dots)$;
 - d. $\delta_{s,j}$ retrieved by means of Eq. (31).
5. Coloured squares highlight the workflow linked to the calibration (red) and to the corrections performed (green) using the assumed real parameter values.
6. The analysis of the results is performed in three different ways.
 - a. The uncertainty propagation of each simulation parameter, x_i , is analysed through the simulated-to-real δ difference, $E_\delta(x_i) = \delta_{s,j} - \delta_r$, varying x_i within its uncertainty range $[x_i - \Delta x_i, x_i + \Delta x_i]$, while all the other parameters are kept. This method is used in Sect. 4.
 - b. The systematic errors of our lidar set-ups are not “randomly distributed”, but are in a fixed state at the time of the measurements. We do not know this fixed state, but assume another fixed set of parameter values (assumed to be real) to correct the systematic errors. Therefore we cannot apply a standard error propagation as for randomly distributed error sources, but determine the depolarization uncertainty $\Delta\delta$ from the minimum and maximum of the simulated δ values: $[\min(\delta_s^{i,j}), \max(\delta_s^{i,j})]$.

Table 2. Values and uncertainties of the synthetic lidar parameters.

Parameters		Value	Uncertainty
\mathbf{I}_L	I_L	1	–
	a_L	0	–
	α	0	$\pm 10^\circ$
\mathbf{M}_E	D_E	0.0	± 0.2
	Δ_E	0°	$\pm 180^\circ$
	β	0°	$\pm 10^\circ$
\mathbf{M}_O	D_O	0.0	± 0.3
	Δ_O	0°	$\pm 180^\circ$
	γ	0.0°	$\pm 5^\circ$
\mathbf{C}	ϕ	$\pm 45^\circ$	–
	ε	0°	$\pm 5^\circ$
\mathbf{M}_S	Ψ	90°	–
	D_T	T_T^P	0.95 ± 0.05
		T_T^S	0.01 ± 0.01
	D_R	T_R^P	0.05 ± 0.05
		T_R^S	0.99 ± 0.01
		η_R	1 –
		η_T	1 –

- c. Finally, we analyse the frequency distribution of the simulated δ values by means of histograms, histogram($\delta_s^{i,j}$), where a displacement towards being larger/smaller than δ_r indicates an over-/underestimation of δ .

4 Depolarization uncertainties of the synthetic lidar

In this section, we define a synthetic lidar system in order to evaluate the error caused by each functional block. We choose the $\Delta 90^\circ$ calibration method implemented by means of a mechanical rotator in front of the PBS. The synthetic lidar system is based on technical specifications of commercial optical devices (Table 2). It is worth noting the large uncertainty of the effective retardance of $\pm 180^\circ$, since this parameter is usually not specified at all by manufacturers and can take any value within this range.

The effect of each simulation parameter x_i is analysed through the difference between the real and the simulated δ ($E_\delta(x_i) = \delta_{s,i} - \delta_r$), varying x_i within its uncertainty range [$x_i - \Delta x_i, x_i + \Delta x_i$], while all the other parameters are kept. This is done for the two real linear depolarization ratios $\delta_r = 0.004$ and 0.45 (Figs. 4–7). Finally, the total systematic error $\Delta\delta$ is determined by $\max(E_\delta) - \min(E_\delta)$ from the complete set of δ simulations (Fig. 8).

4.1 Synthetic lidar: influence of the laser

The laser can introduce errors in the depolarization measurements due to a misalignment angle α of the plane of the

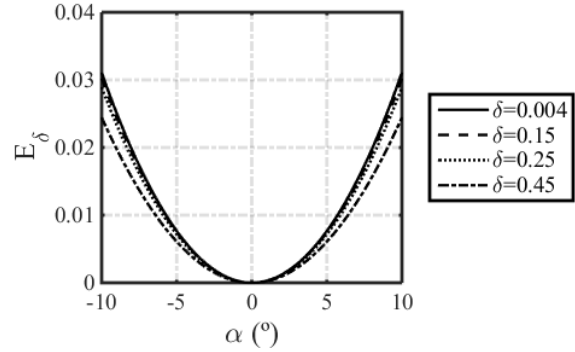


Figure 3. Difference E_δ between the simulated and the real δ , depending on the misalignment angle of the polarizing plane of the laser (α) for different δ values.

laser polarization with respect to the incident plane of the PBS (see Eq. 1). Figure 3 shows E_δ over α with different values of δ_r . As can be seen in Fig. 3, $E_\delta(\alpha)$ increases with α in absolute terms. $\Delta\delta(\alpha)$ ranges between $[0, 0.031]$ and $[0, 0.024]$ for δ values of 0.004 and 0.45 , respectively, showing a low δ dependence. Since the smallest atmospheric δ_m is of the order of 10^{-3} , we assume that $\Delta\delta(\alpha)$ can be neglected ($< 1 \times 10^{-4}$) if α is in the range $0^\circ \pm 0.6^\circ$.

4.2 Synthetic lidar: influence of the emitter optics

\mathbf{M}_E is characterized by the effective diattenuation D_E , the retardance Δ_E , and the rotational misalignment angle β of \mathbf{M}_E with respect to the incident plane of PBS. These parameters are interdependent, and thus Fig. 4 shows the E_δ dependence on Δ_E and D_E for different β . Additionally, the influence of the atmospheric depolarization is assessed for δ_r values: 0.004 and 0.45 in Fig. 4 (top). As aforementioned, Δ_E varies in the range $[-180^\circ, 180^\circ]$ because the retardance of steering and dichroic mirrors is generally not provided in the majority of the technical specifications.

As can be seen in Fig. 4 (top), D_E introduces systematic errors, except for $\beta = 0^\circ$ with $\Delta\delta(D_E, \beta) = [0, 0.001]$. Figure 4 (bottom) shows that the maximum of $E_\delta(\Delta_E, \beta)$ is larger than 0.03 for β larger than 5° in absolute terms, indicating that the lack of information of Δ_E can lead to huge uncertainties even larger than 0.13 for β larger than 10° . Figure 4 shows also that $E_\delta(D_E, \beta)$ and $E_\delta(\Delta_E, \beta)$ decrease with increasing δ values.

In summary, the total $\Delta\delta$ due to the systematic uncertainty of \mathbf{M}_E is $[0, 0.13]$ for $\delta_r = 0.004$ and $[0, 0.1]$ for $\delta_r = 0.45$. It is recommended that the laser beam is emitted directly to the atmosphere to avoid this error source. Otherwise, it is crucial to set $\beta = 0^\circ$ to keep $\Delta\delta(\mathbf{M}_E)$ as low as possible, independently of the effective diattenuation and retardance. For the synthetic lidar set-up, $\beta = 0^\circ \pm 2.5^\circ$ would lead to negligible $E_\delta(D_E, \beta)$ and $E_\delta(\Delta_E, \beta)$ with values lower than 1×10^{-4} .

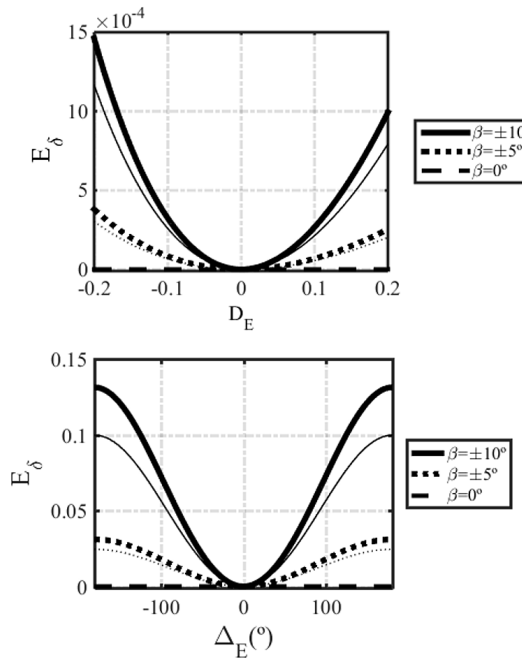


Figure 4. Simulated-to-real δ difference E_δ over the diattenuation D_E (top) and on the retardance Δ_E (bottom) of the emitter optics, for different misalignment angles (β). Thick and thin lines correspond to δ_r values of 0.004 and 0.45, respectively.

4.3 Synthetic lidar: influence of the receiver optics

The parameters of the receiving optics (\mathbf{M}_O) are the effective diattenuation D_O , retardance Δ_O , and the misalignment angle γ between the receiving optics and the incident plane of the PBS. As in the case of \mathbf{M}_E (β , D_E , Δ_E), the influence of any of these parameters on E_δ is not independent of the others. However, the variation of E_δ with γ is very weak, and thus Fig. 5 (top) depicts E_δ vs. D_O for different δ_r , whereas Fig. 5, bottom, depicts E_δ vs. Δ_O for different γ .

According to Fig. 5, top, the uncertainty of D_O in the range $[-0.3, +0.3]$ has a huge impact on $E_\delta(D_O)$ with errors in the range $[+0.4, -0.2]$ for $\delta_r = 0.45$ and similar relative errors for other δ_r values.

Negative values of D_O cause larger $E_\delta(D_O)$, in absolute terms, than positive ones (e.g. $|E_\delta(D_O = -0.3)| = 0.21$ in contrast to $|E_\delta(D_O = +0.3)| = 0.12$ considering $\delta_r = 0.25$ in both cases) because the parallel signal is stronger than the perpendicular one. In order to make the systematic error caused by \mathbf{M}_O negligible, the uncertainty of D_O should be lower than ± 0.0010 for $E_\delta(D_O) < 10^{-4}$, which is a very small value compared to what is available on the market. Thus, we advise the use of accurate calibration methods which can correct for D_O , or to measure this value accurately.

Figure 5 (bottom) shows that the effect of the uncertainty in the retardance $E_\delta(\Delta_O)$ is comparable to that of the emitter block $E_\delta(\Delta_E)$ with $E_\delta(\Delta_O)$ larger than 0.03 for $\gamma = \pm 5^\circ$.

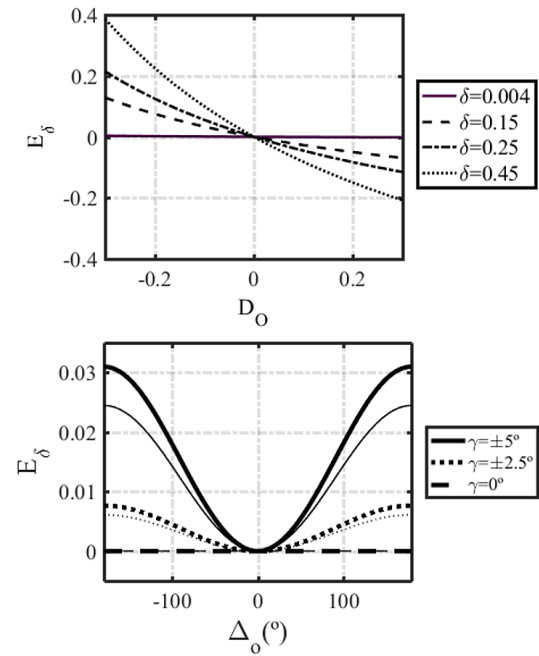


Figure 5. Simulated-to-real δ difference E_δ over the diattenuation D_O for different δ_r values (top) and on the retardance Δ_O of the receiving optics for different misalignment angles γ (bottom). Thick and thin lines correspond to δ_r values of 0.004 and 0.45, respectively.

Therefore, it is recommended that γ is kept as small as possible with little uncertainty.

Summarising, the uncertainties of γ and D_O have a huge impact on $\Delta\delta$, and thus, it is very important to carefully determine these parameters of the receiving optics.

4.4 Synthetic lidar: influence of the polarization splitter

For the synthetic lidar, we consider a non-cleaned polarizing beam splitter which has T_T^P , T_R^P , T_T^S , and T_R^S values and uncertainties as shown in Table 2. Since $T_T^P + T_R^P = 1$ and $T_T^S + T_R^S = 1$, T_T^P , T_R^P , T_T^S , and T_R^S , and their uncertainties are not independent. We choose T_T^P and T_T^S as the variable parameters, and show E_δ over T_T^P in Fig. 6 for different T_T^S and for δ values of 0.004 and 0.45. Although $\Delta T_T^S = \pm 0.01$ is much smaller than $\Delta T_T^P = \pm 0.05$, it has a stronger influence on $E_\delta(T_T^P, T_T^S)$. The ratio $E_\delta(\Delta T_T^S)/\Delta T_T^S$ is about 8 times the ratio $E_\delta(\Delta T_T^P)/\Delta T_T^P$ (i) because the parallel intensity, detected in the reflected path, is much larger than the perpendicular intensity, and (ii) because T_T^S is small; a small change in T_T^S makes a big difference in the crosstalk from the parallel to the perpendicular signal. The influence of ΔT_T^P on $E_\delta(T_T^P, T_T^S)$ increases and that of ΔT_T^S decreases with increasing δ . The systematic errors due to crosstalk can be avoided by means of a cleaned PBS (see Sect. 2.4).

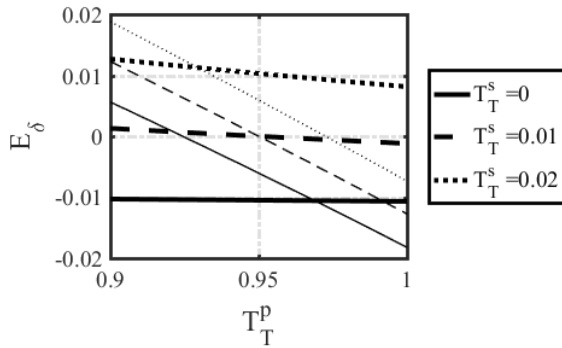


Figure 6. Simulated-to-real δ difference E_δ over the parallel-polarized light transmittance T_T^p for different perpendicular-polarized transmittance T_T^s . Thick and thin lines correspond to δ_r values of 0.004 and 0.45, respectively.

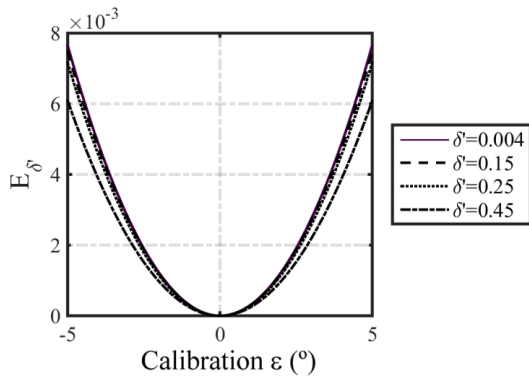


Figure 7. Simulated-to-real δ difference E_δ over the misalignment angle ϵ of the calibrator for different values of δ_r according to the label.

4.5 Synthetic lidar: influence of the calibrator

Here the $\Delta 90^\circ$ calibration with a rotator in front of the PBS is considered. This calibration method is described in Sect. 2.7 (see Freudenthaler, 2016a, for further details). It is worth noting that the uncertainties due to a rotation calibrator affect both calibration and normal measurements, whereas the use of a polarizing filter as calibrator only affects the calibration measurements because it has to be removed for the normal measurement, and hence there is no rotation error ϵ in that.

As can be seen in Fig. 7, $E_\delta(\epsilon)$ is $[0, 0.0008]$ for $\delta_r = 0.004$ and $[0, 0.0006]$ for $\delta_r = 0.45$. Considering the large uncertainty range ($\epsilon = \pm 5^\circ$), $\Delta\delta(\epsilon)$ is really low. Since ϵ is usually smaller in real lidars than in the synthetic lidar, we can conclude that $\Delta\delta(\epsilon)$ can be neglected. This happens because the $\Delta 90^\circ$ calibration method is used, but for other calibration methods, the uncertainty of this parameter needs to be taken into account.

Despite the fact that ϵ does not introduce a considerable systematic error, the position of the calibrator within the lidar

Table 3. Minima and maxima of the simulated volume linear depolarization ratio, δ , from the complete search applied to the synthetic lidar.

Lidar	$\delta = 0.004$		$\delta = 0.45$	
	Min	Max	Min	Max
Synthetic	-0.01	> 1	0.2	> 1

system has to be considered. For example, the $\Delta 90^\circ$ calibration in front of the receiving optics corrects the calibration factor for diattenuation of the receiving optics D_0 but it does not if the calibrator is located behind the receiving optics, as is the case for the LB21, IPRAL, and MUSA lidars (see Table 5).

4.6 Synthetic lidar: total uncertainty analysis

The total systematic error $\Delta\delta$, including all possible mutual dependencies, is determined with a complete grid search of the error space. In order to keep the number of samples around 10^6 , α , D_E , β , γ , and ε are simulated with three values, as e.g. $\alpha = [-10, 0, 10^\circ]$, and Δ_E , D_0 , Δ_O , D_T , and D_R with five values, as e.g. $\Delta_O = [-180^\circ, -90, 0, 90, 180^\circ]$. As a result, there are $3^5 5^5 \cong 7.6 \times 10^5$ simulated δ values. Figure 8 shows the δ histograms for δ_r values of 0.004 (left) and 0.45 (right). The minima and maxima of both histograms are provided in Table 3. For both simulations, the values obtained for δ span over quite a large range reaching even impossible values below the molecular δ (0.004) or δ values larger than 1. Since the distribution of simulated δ is displaced to the right of δ_r , an overestimation of δ is more probable than an underestimation for this synthetic lidar.

5 Systematic depolarization errors of seven EARLINET lidar systems

The PLS is applied to the seven EARLINET lidar systems listed in Table 4, of which POLIS measures the linear depolarization ratio at two wavelengths. Detailed information about the lidar systems is given by Wandinger et al. (2016), except for the upgraded POLIS (Freudenthaler et al., 2016b) and IPRAL (IPSL high-Performance multi-wavelength Raman Lidar for Cloud Aerosol Water Vapor Research) which has recently been deployed at SIRTA atmospheric research observatory (Haeffelin et al., 2005). IPRAL provides measurements at 355 (parallel and perpendicular polarized components), 532, and 1064 nm (elastic backscatter), and the Raman-shifted backscatter at 387 (from N_2), 408 (from H_2O), and 607 nm (from N_2).

Table 5 shows the values and uncertainties of the lidar parameters used for the simulation. The main differences among the lidars are (i) the use of steering optics in the emitter (e.g. MUSA and POLIS do not have this functional

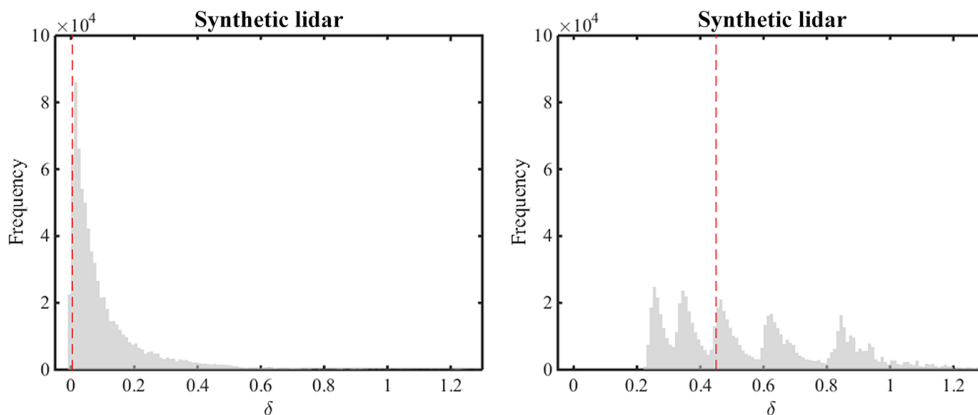


Figure 8. Histogram of the simulated δ values for the synthetic lidar. Dashed lines represent δ_r at 0004 (left) and 045 (right) used in the simulations.

Table 4. EARLINET lidar systems participating in this study.

Lidar name	Institution
LB21-IV-D200	National Technical University of Athens, Greece
LB21-IV-D200	Cyprus University of Technology, Limassol, Cyprus
MULHACEN	CEAMA, University of Granada, Spain
RALI	INOE 2000, Bucharest, Romania
POLLY-XT SEA	TROPOS, Leipzig, Germany
POLIS	LMU Munich, Germany
MUSA	CNR-IMAA, Potenza, Italy
IPRAL	IPSL/SIRTA – CNRS-Ecole Polytechnique, Palaiseau, France

block), (ii) the position and type of the calibrator (e.g. MULHACEN and RALI: polarizer in front of \mathbf{M}_O ; IPRAL and MUSA: half-wave plate in front of M_S), (iii) the type of the polarizing beam splitter \mathbf{M}_S , (iv) the very different values of certain parameters (e.g. $D_O = 0.35$ and $D_O = -0.001$ in MULHACEN and POLIS 355 nm, respectively), and (v) the uncertainty of the retardance Δ_O being negligible for IPRAL and not limited ($\pm 180^\circ$) for all other lidars. It is worth noting that MULHACEN, RALI, and LB21 have been upgraded in the meantime with a cleaned PBS. However, in order to highlight the crosstalk effect, the present analysis is based on the previous lidar configuration.

As the lidar systems have different numbers of free parameters, the number of the complete search samples for each parameter is individually adjusted to provide around 10^6 combinations for each lidar. MULHACEN, RALI, LB21, and POLLY-XT SEA are sampled using three values for α , D_E , β , γ , and ε , that is $[x_i - \Delta x_i, x_i, x_i + \Delta x_i]$, and using five values for Δ_E , D_O , Δ_O , D_T , and D_R , that is $[x_i - \Delta x_i, \dots, x_i, \dots, x_i + \Delta x_i]$ with fixed increments (see more details in Sect. 3), resulting in a total number of combinations of $3^5 5^5 \sim 7.6 \times 10^5$. POLIS and MUSA do not have emitter optics \mathbf{M}_E , and employ a cleaned PBS, wherefore the contributions of D_T and D_R can be neglected. For these systems, the simulation is done with three possible values for

the parameters α , γ , and ε and 193 values for the parameters D_O and Δ_O , resulting in a total number of combinations of $3^3 193^2 \sim 1 \times 10^6$. Finally, for IPRAL, the uncertainties of Δ_O , D_T , and D_R are neglected, and thus α , D_E , β , γ , and ε are simulated with three values, whereas D_O and Δ_E are simulated with 65 values, resulting in $3^5 65^2 \sim 1 \times 10^6$ combinations.

Figures 9 and 10 show the histograms of the simulated δ at $\delta_r = 0.004$ and $\delta_r = 0.45$ for the EARLINET lidars in Table 4. The discontinued distributions for LB21, POLLY-XT SEA, and POLIS show that certain parameters with a big impact are under-sampled. Disregarding the discontinuities, the distributions in the histograms are very different between the lidar systems; some are almost centred Gaussian-like, some more top-hat, and others one-sided, skewed, and strongly peaked. Therefore we only list the minima and maxima of the simulated δ values for each lidar in Table 6.

With the plots in Fig. 11, it is possible to show the contribution of individual parameters to the histograms as coloured sub-histograms. For the case of LB21, the diattenuation parameter of the receiving optics D_O is clearly the dominant error source, and the spread of each sub-histogram shows the combined contribution of the other parameters. In the plot for MULHACEN, with coloured sub-histograms for the three values of the rotation angle of the laser polarization α , we

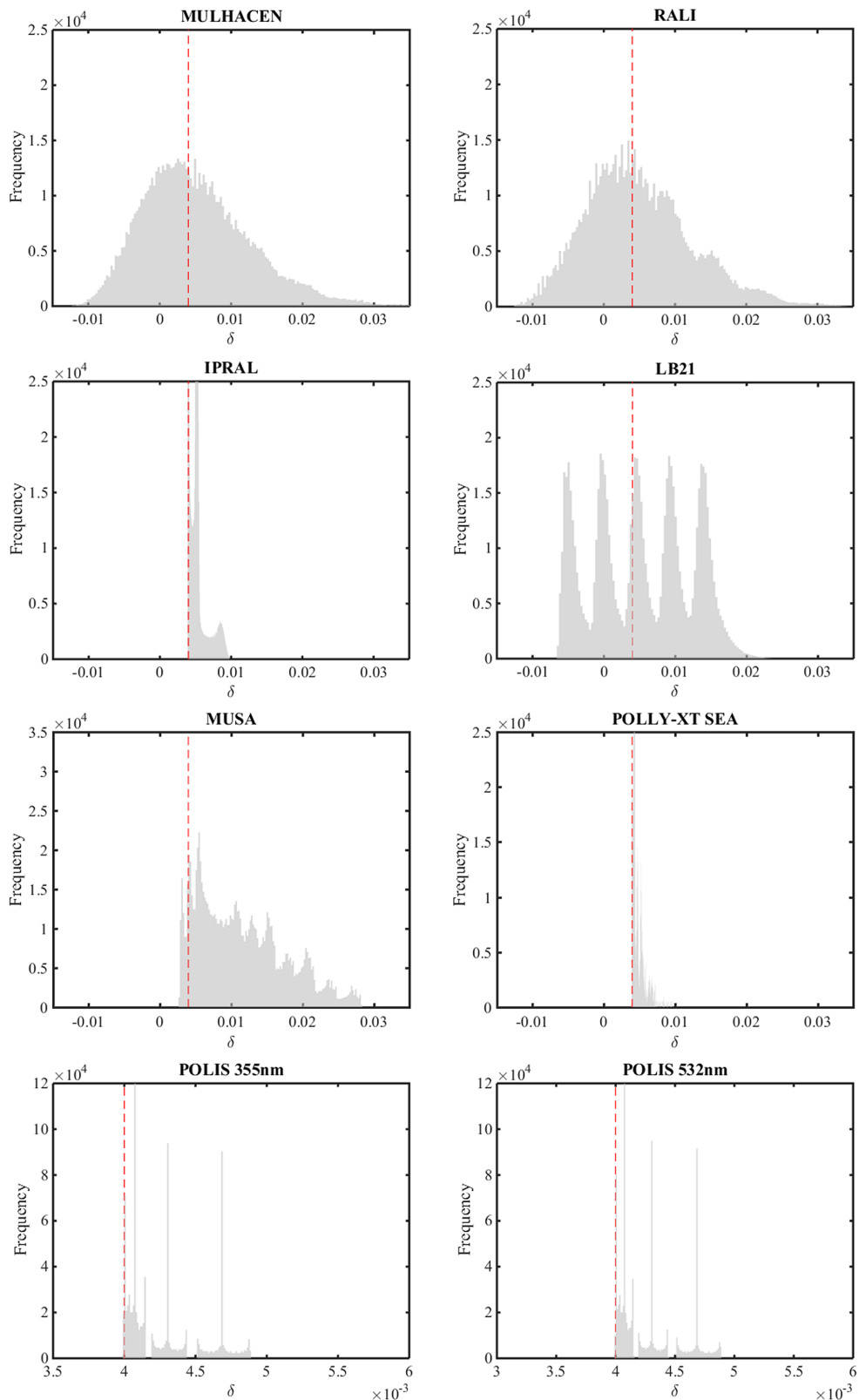


Figure 9. Histogram of the simulated δ values for several EARLINET lidars (Table 4). Dashed lines represent the δ_r at 0004. Please note the expanded x axis for POLIS.

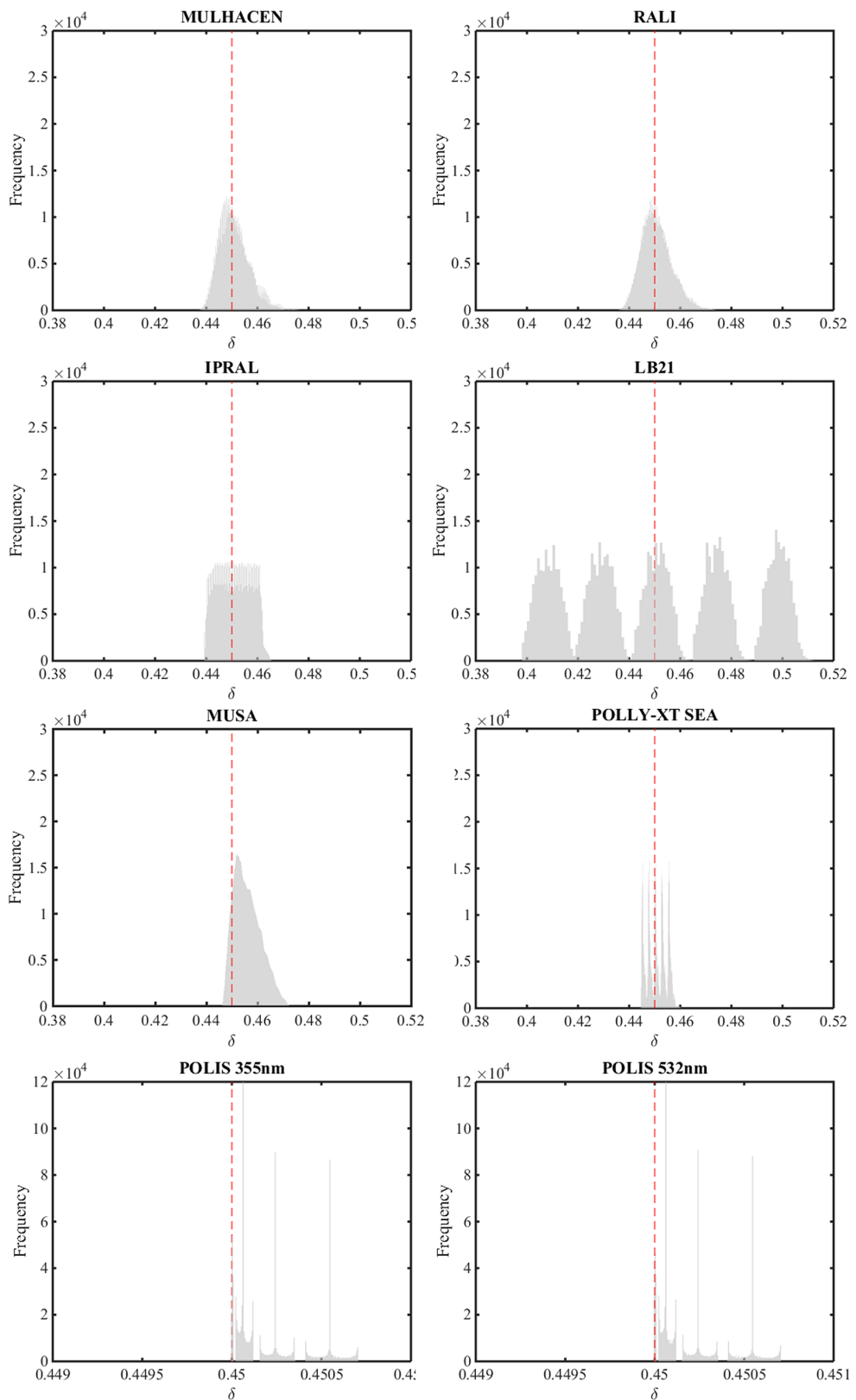


Figure 10. Histogram of the simulated δ values for several EARLINET lidars (Table 4). Dashed lines represent the δ_r at 045. Please note the expanded x axis for POLIS.

Table 5. Values and uncertainties of each lidar parameter for the set of simulated EARLINET lidars. ΔT_T^P and ΔT_T^S are the T_T^P and T_T^S uncertainties. ER is the linear-polarizer extinction ratio.

Property		MULHACEN		RALI		LB21		IPRAL	
		532 nm		532 nm		532 nm		355 nm	
		Value	Uncertainty (\pm)	Value	Uncertainty (\pm)	Value	Uncertainty (\pm)	Value	Uncertainty (\pm)
I_L	α	7.0°	1.0°	8°	0.20°	0°	2.0°	0°	2.0°
M_E	Included	Yes		Yes		Yes		Yes	
	D_E	0.00	0.10	0.00	0.10	0.00	0.05	0.00	0.05
	Δ_E	0°	180°	0°	180°	0°	180°	0°	180°
	β	0.0°	1.0°	0°	1.0°	0°	1.0°	0°	1.0°
M_O	D_O	0.35	0.04	0.2	0.10	0.00	0.05	-0.012	0.012
	Δ_O	0°	180°	0°	180°	0°	180°	0°	-
	γ	0.0°	0.5°	0.0°	0.5°	0.0°	0.5°	0.0°	0.5°
C	Location (in front of) Element	M_O Polarizer		M_O Polarizer		M_S Rotator		M_S 0-order waveplate	
	ε	0.00°	0.10°	0.0°	0.1°	0.0°	0.1°	0.0°	0.1°
M_S	Type Polarizing components	PBS Parallel + perpendicular		PBS Parallel + perpendicular		PBS Parallel + perpendicular		PBS + polarizers Parallel + perpendicular	
	T_T^P	0.95	0.01	0.99	0.01	0.95	0.01	1	-
	T_T^S	0.005	0.001	0.001	0.001	0.01	0.01	0	-
	T_R^P	$1 - T_T^P$	ΔT_T^P	$1 - T_T^P$	ΔT_T^P	$1 - T_T^P$	ΔT_p	0	-
	T_R^S	$1 - T_T^S$	ΔT_T^S	$1 - T_T^S$	ΔT_T^S	$1 - T_T^S$	ΔT_s	1	-
Property		MUSA		POLLY-XT SEA		POLIS 355/532 nm			
		532 nm		532 nm		355 nm		532 nm	
		Value	Uncertainty (\pm)	Value	Uncertainty (\pm)	Value	Uncertainty (\pm)	Value	Uncertainty (\pm)
I_L	α	3.0°	0.6°	0.0°	1.0°	0.0°	0.5°	0.0°	0.5°
M_E	Included	No		Yes		No			
	D_E	-	-	0.00	0.10	-	-	-	-
	Δ_E	-	-	0	180°	-	-	-	-
	β	-	-	0.0°	1.0°	-	-	-	-
M_O	D_O	-0.055	0.003	0.011	0.022	-0.001	0.001	0.011	0.011
	Δ_O	0°	180°	0°	180°	0°	180°	0°	180°
	γ	0°	0.1°	0.0°	0.5°	0.00°	0.10°	0.00°	0.10°
C	Location (in front of) Type	M_S 0-order waveplate		M_O Polarizer		M_O Rotator			
	ε	1.2°	0.3°	3''	3''	0.0°	1.0°	0.0°	1.0°
M_S	Type Polarizing components	PBS + polarizers Parallel + perpendicular		Polarizer Total + perpendicular		PBS + polarizers Parallel + perpendicular			
	T_T^P	1	-	0.532	0.017	0.21	-	0.79	-
	T_T^S	0	-	0.500	0.015	0	-	0	-
	T_R^P	0	-	$ER(1 - T_T^P)$	-	0	-	0	-
	T_R^S	1	-	0.500	0.015	0.225	-	0.8	-

see that the shift between the sub-histograms due to the uncertainty of α accounts for about one-third of the total width of the histogram. The RALI plot, with coloured ε -histograms indistinguishably lying above each other, shows that the uncertainty of ε has a negligible impact on the total error.

The small error of POLIS compared to the other lidars can be attributed to (i) the custom-made dichroic mirrors designed for negligible diattenuation, (ii) the absence of any emitter optics, (iii) the cleaned PBS, and (iv) the well-

adjusted rotation of the laser polarization with small uncertainty (Table 5).

Despite $\Delta\delta$ still being large for some lidars, the comparison with the much larger error of the synthetic lidar shows the success of the effort carried out by the EARLINET community towards the identification of the main error sources and a better characterization of the individual optical elements. From the results of our study, some indications can be provided to reduce the polarization-dependent systematic errors.

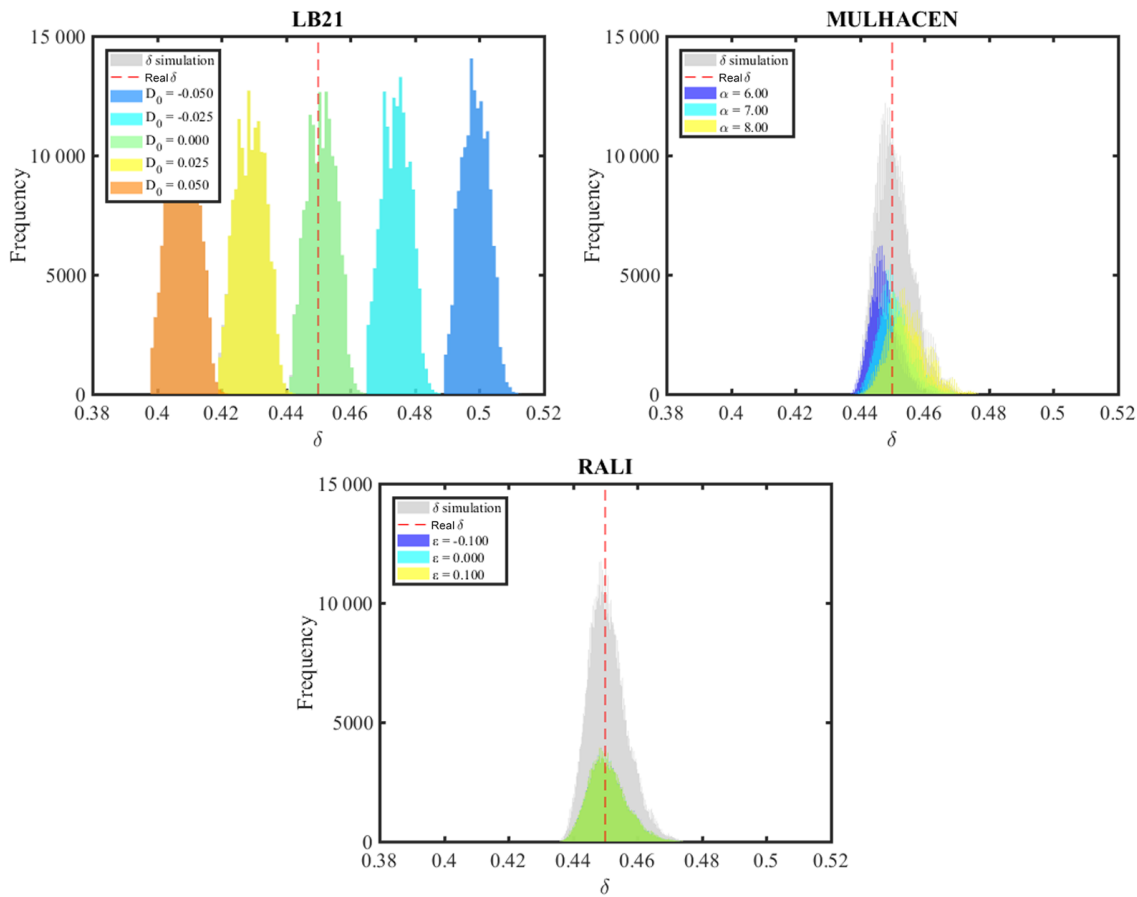


Figure 11. Histogram of the simulated δ values for LB21, MULHACEN, and RALI, with coloured sub-histograms indicating the contribution at certain parameter values of α , D_0 , and ε values. Dashed lines represent δ_r at 045.

Table 6. Minima and maxima of the simulated δ for the EARLINET lidar systems at $\delta_r = 0004$ and $\delta_r = 045$. $\Delta\delta$ is the minimum and maximum range.

Lidar	$\delta = 0.004$		$\delta = 0.45$	
	Min	Max	Min	Max
MULHACEN	-0.012	0.039	0.437	0.477
RALI	-0.012	0.034	0.436	0.474
LB21	-0.006	0.024	0.399	0.512
IPRAL	0.0039	0.0098	0.4393	0.4654
MUSA	0.003	0.028	0.446	0.472
POLLY-XT SEA	0.0039	0.0096	0.4446	0.4602
POLIS	355 nm	0.004	0.0049	0.45
	532 nm	0.004	0.0049	0.45
			0.4507	

The polarization purity of the laser beam can be improved by using a high-energy polarizer after the emitting optics. To reduce the uncertainty introduced by M_E , it is highly recommended that emitter optics is avoided. The errors due to the emitter and receiver optics can be reduced by improving

their rotational alignment (i.e. β and γ) with respect to the polarizing beam splitter. Finally, the PBS cross-talk can be removed by using a cleaned PBS. Additionally, a good characterization of the parameters and consequential correction can drastically reduce the systematic error. For example, the α and D_0 values can be determined by experimental assessments, as indicated by Freudenthaler (2016a).

6 Conclusions

This work shows the numerical analysis of the polarization-related systematic errors of the linear depolarization ratio δ of one synthetic and seven EARLINET lidar systems, which all use one of the $\Delta 90$ calibration techniques described by Freudenthaler (2016a). It uses the lidar model described there to apply corrections to the signals and calibrations with assumed real parameter values. For the error estimation we use a complete grid scan over all relevant error sources.

The results for the synthetic lidar showed that for real δ (δ_r) values of 0.004 and 0.45, the measured δ could range between $[-0.025, 1.1064]$ and $[0.386, 1.021]$, respectively.

From this simulation we conclude that the systematic error can be very large if the lidar system is not well characterized and aligned.

Within the ranges of the typical uncertainties, the diattenuation of the receiving optics and of the polarizing beam splitter have the biggest impact. The next important parameters are the retardance of the emitting and of the receiving optics, and the rotational misalignment between the plane of polarization of the laser and the incident plane of the PBS.

The simulations of the EARLINET lidars show possible measured values of δ in the range of $[-0.012, 0.039]$ for a δ_r of 0.004 and in the range of $[0.399, 0.512]$ for a δ_r of 0.45. Compared to the large error of the synthetic lidar that is not well-characterized, this is a big improvement.

The uncertainty of some parameters, as the retardance of dichroic mirrors, is still very large, often because the manufacturers of optics do not provide specific information. The numerical error analysis shown in this work is actually a sensitivity analysis, which can be used to identify the parameters that need more accurate characterization. A positive example for such an improvement is the receiving optics of IPRAL, which employs custom-made dichroic beam splitters with almost negligible diattenuation and 0° retardance.

Finally, further investigations are still required for a better understanding of the polarization effects of large windows, special lenses, and Newtonian telescopes. Possible evidence of error sources not considered in this work is if δ values are measured outside of the simulated δ distribution. For example, elliptical polarization of the outgoing laser beam could strongly affect the δ determination.

7 Data availability

The polarimetric lidar simulator and simulations supporting this article are available upon request from the corresponding author.

Appendix A: Explanation of the influence of a linear polarizer sheet, which is not well aligned, being placed behind the PBS to “clean” the crosstalk

From the Müller matrix \mathbf{M}_S of the PBS and a polarizing sheet filter (polarization analyzer \mathbf{M}_A), which is rotated by an angle ϕ from the nominal orientation, we get the first row vector indicated by $(|)$ (see Freudenthaler, 2016a, Sect. 3.1 and Eqs. (S.10.10.1 ff.) in the Supplement).

$$\frac{\langle \mathbf{M}_A(\phi) \mathbf{M}_S |}{T_A T_S} = \begin{pmatrix} 1 + c_{2\phi} D_A D_S & D_S + c_{2\phi} D_A & s_{2\phi} D_A Z_S c_S & s_{2\phi} D_A Z_S s_S \end{pmatrix}$$

The transmittances for p - and s -polarized light, T^P and T^S , respectively, are

$$\begin{aligned} T_{AS}^P &= T_A T_S (1 + c_{2\phi} D_A D_S) + (D_S + c_{2\phi} D_A) \\ &= (1 + D_S) (1 + c_{2\phi} D_A) \\ T_{AS}^S &= T_A T_S (1 + c_{2\phi} D_A D_S) - (D_S + c_{2\phi} D_A) \\ &= (1 - D_S) (1 - c_{2\phi} D_A), \end{aligned}$$

and the extinction ratio ρ_{AT} for the transmitted path is

$$\begin{aligned} \rho_{AT} &= \frac{T_{AT}^S}{T_{AT}^P} = \frac{(1 - D_T) (1 - c_{2\phi} D_A)}{(1 + D_T) (1 + c_{2\phi} D_A)} = \rho_T \frac{1 - c_{2\phi} D_A}{1 + c_{2\phi} D_A} \\ &= \rho_T \frac{(T_A^P + T_A^S) - c_{2\phi} (T_A^P - T_A^S)}{(T_A^P + T_A^S) + c_{2\phi} (T_A^P - T_A^S)} = \rho_T \frac{(1 + \rho_A) - c_{2\phi} (1 - \rho_A)}{(1 + \rho_A) + c_{2\phi} (1 - \rho_A)} \\ &= \rho_T \frac{1 - c_{2\phi} + \rho_A (1 + c_{2\phi})}{1 + c_{2\phi} + \rho_A (1 - c_{2\phi})} = \rho_T \frac{\tan^2 \phi + \rho_A}{1 + \rho_A \tan^2 \phi} \\ &\approx \rho_T \rho_A \left(1 + \frac{\tan^2 \phi}{\rho_A} \right). \end{aligned}$$

Please note that p - and s -polarizations are with respect to the incidence plane of the polarizing beam-splitter cube \mathbf{M}_S , and that the polarizing sheet filter is rotated by an angle of 90° in the reflected path, with $\cos(2 \cdot (90^\circ + \phi)) = \cos(2\phi)$. The extinction ratio ρ_{AR} for the reflected path can be derived in the same way:

$$\rho_{AR} = \frac{T_{AR}^S}{T_{AR}^P} = \rho_R \frac{\tan^2 \phi + \rho_A}{1 + \rho_A \tan^2 \phi} \approx \rho_R \rho_A \left(1 + \frac{\tan^2 \phi}{\rho_A} \right).$$

For a typical polarizing beam-splitter cube with $T_T^P = 0.95$, $T_R^S = 0.99$, and $T_T^S = 1 - T_R^S$, $T_R^P = 1 - T_T^P$, the extinction ratio in the transmitted path is $\rho_T = T_T^S / T_T^P = 0.05$ and in the reflected path is $\rho_R = T_R^P / T_R^S = 0.01$. Using additional cleaning polarizing sheet filters with $\rho_A = 0.01$, the combined extinction ratios $\rho_{AS} = \rho_A \cdot \rho_S$ are improved by a factor of 100. A misalignment of the polarizing sheet filter by an angle ϕ with $\tan^2 \phi = \rho_A$, for example, decreases the improvement by a factor of 2, which is, in this case, about $\phi = 5.7^\circ$ (for $\rho_A = 0.01$).

Acknowledgements. This work was supported by the Andalusia regional government through projects P12-RNM-2409 and P10-RNM-6299 and by the Spanish Ministry of Science and Technology through projects CGL2010-18782 and CGL2013-45410-R. The financial support for EARLINET in the ACTRIS Research Infrastructure Project by the European Union's Horizon 2020 research and innovation programme under grant agreement no. 654169 and previously under grant agreement no. 262254 in the Seventh Framework Programme (FP7/2007-2013) is gratefully acknowledged. This work was also supported by the University of Granada through the contract "Plan Propio. Programa 9. Convocatoria 2013" and the grant AP2009-0559.

Edited by: A. Ansmann

Reviewed by: F. Cairo and one anonymous referee

References

- Álvarez, J. M., Vaughan, M. A., Hostetler, C. A., Hunt, W. H., and Winker, D. M.: Calibration technique for Polarization-Sensitive Lidars, *J. Atmos. Ocean. Tech.*, 23, 683–699, doi:10.1175/JTECH1872.1, 2006.
- Ansmann, A., Mattis, I., Müller, D., Wandinger, U., Radlach, M., Althausen, D., and Damoah, R.: Ice formation in Saharan dust over central Europe observed with temperature/humidity/aerosol Raman lidar, *J. Geophys. Res.-Atmos.*, 110, , D18S12, doi:10.1029/2004JD005000, 2005.
- Ansmann, A., Tesche, M., Seifert, P., Gross, S., Freudenthaler, V., Apituley, A., Wilson, K. M., Serikov, I., Linne, H., Heinold, B., Hiebsch, A., Schnell, F., Schmidt, J., Mattis, I., Wandinger, U., and Wiegner, M.: Ash and fine-mode particle mass profiles from EARLINET-AERONET observations over central Europe after the eruptions of the Eyjafjallajökull volcano in 2010, *J. Geophys. Res.-Atmos.*, 116, D00U02, doi:10.1029/2010JD015567, 2011.
- Bissonette, L. R and Roy, G.: Range-height scans of Lidar depolarization for characterizing properties and phase of clouds and precipitation, *J. Atmos. Ocean. Tech.*, 18, 1429–1446, doi:10.1175/1520-0426(2001)018<1429:RHSOLD>2.0.CO;2, 2001.
- Bravo-Aranda, J. A., Navas-Guzmán, F., Guerrero-Rascado, J. L., Pérez-Ramírez, D., Granados-Muñoz, M. J., and Alados-Arboledas, L.: Analysis of lidar depolarization calibration procedure and application to the atmospheric aerosol characterization, *Int. J. Remote Sens.*, 34, 3543–3560, doi:10.1080/01431161.2012.716546, 2013.
- Bravo-Aranda, J. A., Titos, G., Granados-Munoz, M. J., Guerrero-Rascado, J. L., Navas-Guzman, F., Valenzuela, A., Lyamani, H., Olmo, F. J., Andrey, J., and Alados-Arboledas, L.: Study of mineral dust entrainment in the planetary boundary layer by lidar depolarisation technique, *Tellus B*, 67, 26180, doi:10.3402/tellusb.v67.26180, 2015.
- Cairo, F., Di Donfrancesco, Adriani, A., Pulvirenti L., and Fierli, F.: Comparison of various linear depolarization parameters measured by lidar, *Appl. Optics*, 38, 4425–4432, doi:10.1364/AO.38.004425, 1999.
- Chaikovsky, A. P., Dubovik, O., Holben, B. N., and Bril, A. I.: Methodology to retrieve atmospheric aerosol parameters by combining ground-based measurements of multi-wavelength lidar and sun sky-scanning radiometer, Eighth International Symposium on Atmospheric and Ocean Optics: Atmospheric Physics, 4678, 257–268, doi:10.11117/12.458450, 2002.
- Chipman, R. A.: Mueller matrices, in: *Handbook of Optics*, edited by: Bass, M., Volume I (3rd Edition), Chap. 14, McGraw-Hill, ISBN-13: 978-0071498890, 2009.
- Clark, N. and Breckinridge, J. B.: Polarization compensation of Fresnel aberrations in telescopes, *Uv/Optical/Ir Space Telescopes and Instruments: Innovative Technologies and Concepts V*, 81460, Report/Patent No.: NF1676L-12395, doi:10.11117/12.896638, 2011.
- David, G., Miffre, A., Thomas, B., and Rairoux, P.: Sensitive and accurate dual-wavelength UV-VIS polarization detector for optical remote sensing of tropospheric aerosols, *Appl. Phys B*, 108, 197–216, doi:10.1007/s00340-012-5066-x, 2012.
- Di, H., Hua, D., Yan, L., Hou, X. and Wei, X.: Polarization analysis and corrections of different telescopes in polarization lidar, *Appl. Opt., OSA*, 54, 389–397, doi:10.1364/AO.54.000389, 2015.
- Engelmann, R., Kanitz, T., Baars, H., Heese, B., Althausen, D., Skupin, A., Wandinger, U., Komppula, M., Stachlewska, I. S., Amiridis, V., Marinou, E., Mattis, I., Linné, H., and Ansmann, A.: The automated multiwavelength Raman polarization and water-vapor lidar PollyXT: the neXT generation, *Atmos. Meas. Tech.*, 9, 1767–1784, doi:10.5194/amt-9-1767-2016, 2016.
- Freudenthaler, V., Esselborn, M., Wiegner, M., Heese, B., Tesche, M., Ansmann, A., Müller, D., Althausen, D., Wirth, M., Fix, A., Ehret, G., Knippertz, P., Toledano, C., Gasteiger, J., Garhammer, M., and Seefeldner, M.: Depolarization ratio profiling at several wavelengths in pure Saharan dust during SAMUM 2006, *Tellus B*, 61, 165–179, doi:10.1111/j.1600-0889.2008.00396.x, 2009.
- Freudenthaler, V.: About the effects of polarising optics on lidar signals and the $\Delta\Theta$ -calibration, *Atmos. Meas. Tech. Discuss.*, doi:10.5194/amt-2015-338, in review, 2016a.
- Freudenthaler, V., Seefeldner, M., Groß, S., and Wandinger, U.: Accuracy of Linear Depolarisation Ratios in Clean Air Ranges Measured with POLIS-6 at 355 and 532 nm, *EPJ Web of Conferences*, 119, 25013, doi:10.1051/epjconf/201611925013, 2016b.
- Gimmestad, G. G.: Reexamination of depolarization in lidar measurements. *Appl. Optics*, 47, 3795–3802, doi:10.1364/AO.47.003795, 2008.
- Granados-Muñoz, M. J., Guerrero-Rascado J. L., Bravo-Aranda, J. A., Navas-Guzmán, F., Valenzuela, A., Lyamani, H., Chaikovsky, A., Wandinger, U., Ansmann, A., Dubovik, O., Grudo, J. O., and Alados-Arboledas L.: Retrieving aerosol microphysical properties by Lidar-Radiometer Inversion Code (LIRIC) for different aerosol types, *J. Geophys. Res. Atmos.*, 119, 4836–4858, doi:10.1002/2013JD021116, 2014.
- Groß, S., Tesche, M., Freudenthaler, V., Toledano, C., Wiegner, M., Ansmann, A., Althausen, D., and Seefeldner, M.: Characterization of Saharan dust, marine aerosols and mixtures of biomass-burning aerosols and dust by means of multi-wavelength depolarization and Raman lidar measurements during SAMUM 2, *Tellus B*, 63, 706–724, doi:10.1111/j.1600-0889.2011.00556.x, 2011.
- Groß, S., Freudenthaler, V., Wiegner, M., Gasteiger, J., Geiss, A., and Schnell, F.: Dual-wavelength linear depolarization ratio of volcanic aerosols: Lidar measurements of the Eyjafjallajökull plume over Maisach, Germany, *Atmos. Environ.*, 48, 85–96, doi:10.1016/j.atmosenv.2011.06.017, 2012.

- Groß, S., Esselborn, M., Weinzierl, B., Wirth, M., Fix, A., and Petzold, A.: Aerosol classification by airborne high spectral resolution lidar observations, *Atmos. Chem. Phys.*, 13, 2487–2505, doi:10.5194/acp-13-2487-2013, 2013.
- Groß, S., Freudenthaler, V., Schepanski, K., Toledano, C., Schäfler, A., Ansmann, A., and Weinzierl, B.: Optical properties of long-range transported Saharan dust over Barbados as measured by dual-wavelength depolarization Raman lidar measurements, *Atmos. Chem. Phys.*, 15, 11067–11080, doi:10.5194/acp-15-11067-2015, 2015.
- Guerrero-Rascado, J. L., Ruiz, B., and Alados-Arboledas, L.: Multi-spectral Lidar characterization of the vertical structure of Saharan dust aerosol over southern Spain. *Atmos. Environ.*, 42, 2668–2681, doi:10.1016/j.atmosenv.2007.12.062, 2008.
- Haefelin, M., Barthès, L., Bock, O., Boitel, C., Bony, S., Bouniol, D., Chepfer, H., Chiriaco, M., Cuesta, J., Delanoë, J., Drobinski, P., Dufresne, J.-L., Flamant, C., Grall, M., Hodzic, A., Hourdin, F., Lapouge, F., Lemaître, Y., Mathieu, A., Morille, Y., Naud, C., Noël, V., O’Hirok, W., Pelon, J., Pietras, C., Protat, A., Romand, B., Scialom, G., and Vautard, R.: SIRTA, a ground-based atmospheric observatory for cloud and aerosol research, *Ann. Geophys.*, 23, 253–275, doi:10.5194/angeo-23-253-2005, 2005.
- Hayman, M. and Thayer, J. P.: General description of polarization in lidar using Stokes vectors and polar decomposition of Mueller matrices, *J. Opt. Soc. Am. A*, 29, 400–409, doi:10.1364/JOSAA.29.000400, 2012.
- Lam, W. S. T and Chipman R.: Balancing polarization aberrations in crossed fold mirrors, *Appl. Optics*, 54, 3236–3245, doi:10.1364/AO.54.003236, 2015.
- Lu, S.-Y. and Chipman, R. A.: Interpretation of Mueller matrices based on polar decomposition, *J. Opt. Soc. Am. A*, 13, 1106–1113, 1996.
- Mamouri, R. E. and Ansmann, A.: Fine and coarse dust separation with polarization lidar, *Atmos. Meas. Tech.*, 7, 3717–3735, doi:10.5194/amt-7-3717-2014, 2014.
- Mattis, I., Tesche, M., Grein, M., Freudenthaler, V., and Muller, D.: Systematic error of lidar profiles caused by a polarization-dependent receiver transmission: quantification and error correction scheme, *Appl. Optics*, 48, 2742–2751, doi:10.1364/AO.48.002742, 2009.
- Mishchenko, M. I. and Hovenier, J. W.: Depolarization of light backscattering by randomly oriented nonspherical particles, *Opt. Lett.*, 20, 1356–1358, doi:10.1364/OL.20.001356, 1995.
- Navas-Guzman, F., Muller, D., Bravo-Aranda, J. A., Guerrero-Rascado, J. L., Granados-Munoz, M. J., Perez-Ramirez, D., Olmo, F. J., and Alados-Arboledas, L.: Eruption of the Eyjafjallajokull Volcano in spring 2010: Multiwavelength Raman lidar measurements of sulphate particles in the lower troposphere, *J. Geophys. Res.-Atmos.*, 118, 1804–1813, doi:10.1002/jgrd.50116, 2013a.
- Navas-Guzmán, F., Bravo-Aranda, J. A., Guerrero-Rascado, J. L., Granados-Muñoz, M. J., and Alados-Arboledas, L.: Statistical analysis of aerosol optical properties retrieved by Raman lidar over Southeastern Spain, *Tellus B*, 65, 21234, doi:10.3402/tellusb.v65i0.21234, 2013b.
- Nemuc, A., Vasilescu, J., Talianu, C., Belegante, L., and Nicolae, D.: Assessment of aerosol’s mass concentrations from measured linear particle depolarization ratio (vertically resolved) and simulations, *Atmos. Meas. Tech.*, 6, 3243–3255, doi:10.5194/amt-6-3243-2013, 2013.
- Pappalardo, G., Amodeo, A., Pandolfi, M., Wandinger, U., Ansmann, A., Bösenberg, J., Matthias, V., Amiridis, V., De Tomasi, F., Frioud, M., Larlori, M., Komguem, L., Papayannis, A., Roca-denbosch, F., and Wang, X.: Aerosol lidar intercomparison in the framework of the EARLINET project. 3. Raman lidar algorithm for aerosol extinction, backscatter, and lidar ratio. *Appl. Opt.*, 43, 5370–5385, doi:10.1364/AO.43.000977, 2004.
- Reichardt, J., Baumgart, R., and McGee, T. J.: Three-signal methods for accurate measurements of depolarization ratio with lidar, *Appl. Optics*, 42, 4909–4913, doi:10.1364/AO.42.004909, 2003.
- Samaras, S., Nicolae, D., Böckmann, C., Vasilescu, J., Binietoglou, I., Labzovskii, L., Toanca, F., Papayannis, A.: Using Raman-lidar-based regularized microphysical retrievals and Aerosol Mass Spectrometer measurements for the characterization of biomass burning aerosols, *J. Comput. Phys.*, 299, 156–174, doi:10.1016/j.jcp.2015.06.045, 2015.
- Schotland, R. M., Sassen, K., and Stone, R.: Observations by Lidar of Linear Depolarization Ratios for Hydrometeors, *J. Appl. Meteorol.*, 10, 1011–1017, doi:10.1175/1520-0450(1971)010<1011:OBLOLD>2.0.CO;2, 1971.
- Snels, M., Cairo, F., Colao, F., and Di Donfrancesco, G.: Calibration method for depolarization lidar measurements, *Int. J. Remote Sens.*, 30, 5725–5736, doi:10.1080/01431160902729572, 2009.
- van de Hulst, H. C.: Light scattering by small particles, John Wiley & Sons, Inc., New York, ISBN-13: 139780486642284, 1957.
- Wagner, J., Ansmann, A., Wandinger, U., Seifert, P., Schwarz, A., Tesche, M., Chaikovsky, A., and Dubovik, O.: Evaluation of the Lidar/Radiometer Inversion Code (LIRIC) to determine microphysical properties of volcanic and desert dust, *Atmos. Meas. Tech.*, 6, 1707–1724, doi:10.5194/amt-6-1707-2013, 2013.
- Wandinger, U., Freudenthaler, V., Baars, H., Amodeo, A., Engelmann, R., Mattis, I., Groß, S., Pappalardo, G., Giunta, A., D’Amico, G., Chaikovsky, A., Osipenko, F., Slesar, A., Nicolae, D., Belegante, L., Talianu, C., Serikov, I., Linné, H., Jansen, F., Apituley, A., Wilson, K. M., de Graaf, M., Trickl, T., Giehl, H., Adam, M., Comerón, A., Muñoz-Porcar, C., Roca-denbosch, F., Sicard, M., Tomás, S., Lange, D., Kumar, D., Pujadas, M., Molero, F., Fernández, A. J., Alados-Arboledas, L., Bravo-Aranda, J. A., Navas-Guzmán, F., Guerrero-Rascado, J. L., Granados-Muñoz, M. J., Preißler, J., Wagner, F., Gausa, M., Grigorov, I., Stoyanov, D., Iarlori, M., Rizi, V., Spinelli, N., Boselli, A., Wang, X., Lo Feudo, T., Perrone, M. R., De Tomasi, F., and Burlizzi, P.: EARLINET instrument intercomparison campaigns: overview on strategy and results, *Atmos. Meas. Tech.*, 9, 1001–1023, doi:10.5194/amt-9-1001-2016, 2016.